

Article

Grid Voltage Estimation Based on Integral Resonant Current Controller for LCL-Filtered Grid-Connected Inverter without AC Voltage Sensors

Thuy Vi Tran  and Kyeong-Hwa Kim * 

Department of Electrical and Information Engineering, Research Center for Electrical and Information Technology, Seoul National University of Science and Technology, 232 Gongneung-ro, Nowon-gu, Seoul 01811, Korea; tranvithuy@gmail.com

* Correspondence: k2h1@seoultech.ac.kr; Tel.: +82-2-970-6406; Fax: +82-2-978-2754

Received: 13 November 2020; Accepted: 1 December 2020; Published: 2 December 2020



Abstract: A high reliability of a grid-connected inverter (GCI) system at reasonable cost is a critical requirement for maximizing renewable energy potential in the electrical energy market. Several grid voltage sensorless control approaches have been investigated not only to eliminate the vulnerability of faulty sensors but also to further reduce the GCI commercial price. In this paper, a frequency adaptive integral-resonant full-state feedback current control scheme with the facilitation of a full-state observer is adopted for a grid-connected inductive–capacitive–inductive (LCL) filtered inverter without sensing the grid voltages. The proposed scheme actively damps the filter resonance and ensures the robustness of the inverter system against unexpected severe grid conditions with low cost and simplified hardware construction. The synchronization of the inverter with the main grid is accomplished by the proposed current controller-based grid voltage estimator, in which the grid frequency and phase angle can be detected effectively. In addition, the actual grid voltages are precisely regenerated to ensure the stable performance of the full-state observer. A safe start-up procedure is also presented for the grid voltage sensorless control of the LCL-filtered inverter to avoid a critical overcurrent and long settling time during the start-up instant, offering a stable and reliable inverter system operation with low computational burden. The effectiveness and feasibility of the proposed voltage sensorless current control scheme are validated by the simulation and experimental results under non-ideal grid conditions such as the harmonic distortion, grid frequency variation, and sudden grid phase angle jump.

Keywords: distorted grid; frequency adaptation; grid-connected inverter; LCL filter; phase angle jump; voltage sensorless control

1. Introduction

Voltage source inverters (VSIs) are typically used as an interface between the main grid and renewable distributed generation (DG) sources. By regulating the injected grid currents using a proper current control strategy, the maximized active power extracted from the DG can be delivered to the grid. Because the pulse width modulation (PWM) technique with a high switching frequency is commonly adopted for the inverter topologies, inductive (L) or inductive–capacitive–inductive (LCL) filters are a mandatory part in inverter structures to eliminate the switching harmonics injected into the grid. Among them, the LCL filter configuration is preferred because of its superiority of high switching frequency attenuation with a small and compact size in comparison with the L filter giving a similar performance. However, the undamped resonance nature of the LCL filter requires a robust control algorithm to stabilize the system. The damping issue in the LCL-filtered inverter can be solved simply

by a passive solution using additional resistors in LCL circuits at the expense of higher power loss [1]. On the other hand, active damping methods based on the modified control algorithm or additional LCL filter state feedback are preferable [2–5]. In particular, the research works in [2,3] install additional sensors for the capacitor currents or voltages to accomplish the virtual-resistor-based active damping solution. Alternatively, the full-state feedback control method is studied for an LCL-filtered inverter system in detail in [4,5] to actively damp the resonance peak. To save the cost of sensing devices for all system states, a full-state observer to estimate the system state variables is used in those works.

Controlling an LCL-filtered inverter while reducing the total cost and hardware complexity has gained considerable research attention recently. Further elimination of the sensor is feasible if the software-based methods in sensorless control approach can replace the measurement signals by the sensor without harming the system's reliable operation. In the grid-connected inverter (GCI), the direct current (DC)-link voltage and grid-side current sensors should be installed for the purpose of protection and output regulation, while the grid voltage sensors ensure an accurate synchronization between the inverter and grid to maximize the injected active power. However, if the grid voltage information is effectively extracted by alternative methods, the grid voltage sensors can be safely removed in the inverter system. Generally, there are several approaches to estimate the grid voltages, such as the direct calculation from the system model [6], virtual-flux-based grid voltage estimation [7,8], power model-based grid voltage estimation [9], observer-based grid voltage estimation [2,5,10,11], and grid voltage estimation from control-structure dependent methods [12–18]. All these methods have both advantages and disadvantages.

In particular, the study in [6] applies a simple approach to obtain the grid voltages directly from the mathematical relation between the inverter voltages, sensed currents, and filter parameters. However, the calculation of the voltage drop across the inductors requires the differentiation of the currents, which amplifies the measurement noise. Since using a pure integrator in the virtual-flux-based method still exposes a problem of DC drift, the studies in [7,8] implement a low pass filter to reduce the unexpected DC drift with a cost of slow dynamic response. Other studies construct disturbance estimators in parallel with the current controllers to estimate the grid voltage information [2,5,10,11]. In [2], even though the grid voltage sensors are successfully removed in the LCL-filtered inverter, this scheme requires the direct measurements of both the inverter-side and grid-side currents to realize the capacitor currents. The research in [5,10] proposes a comprehensive voltage sensorless solution for the LCL-and L-filtered inverter based on an adaptive neural network, respectively. However, the implementation of [10] requires information of the actual grid frequency, whereas the performance of the scheme in [5] is still dependent on the slow dynamic of a phase-locked loop used to estimate the grid phase angle. Another approach to obtain the grid voltage information by the model-based observer is presented in [11] at the expense of high computational burden.

As an alternative to building a separate estimator for the grid voltages, several control schemes develop the grid voltage estimation based on the current controller to further reduce the computational burden. The studies in [15,16] extract the grid voltage information by implementing an additional proportional-integral (PI) or resonant controller with the current error as the control input in the synchronous reference frame (SRF) or stationary frame, respectively. Rather than utilizing the current controller, in [17], the grid frequency and phase angle in a three phase PWM converter are obtained by the output of the PI controller for the DC-link voltage control loop.

All the above schemes in [15–17] are devised for the L-filter inverter. The research work in [18] directly feeds the inverter voltage to the phase-locked loop to extract the phase angle for the synchronization purpose of an LCL-filtered inverter. Even though the scheme is simple, the phase shift between the inverter voltage and the actual grid voltage is unavoidable. To solve this problem, the research in [12] utilizes the output of the resonant current controller to first estimate the frequency and phase angle of the inverter voltage, which are added with a compensator factor to obtain the grid phase angle. The studies in [13,14] present a novel algorithm to extract the grid voltage information by modifying the PI or proportional-resonant (PR) current regulator in the SRF or stationary frame,

respectively. To obtain the high precision of estimated phase angle and frequency, the angle error which is obtained from the output of the current controller is used to drive a grid voltage observer. However, since those schemes are applied to an L-filtered inverter only, further development should be conducted to apply them to an LCL-filtered inverter.

The grid voltage sensorless control scheme commonly raises major concerns for the user about the operation reliability, especially during the start-up instant. However, only a few start-up methods are mentioned in the existing voltage sensorless solutions [7,10,11,13–15,18]. In this regard, the accurate information of actual grid phase angle and grid voltage magnitude are essential to ensure a smooth start-up with low overshoot of injected currents as well as short settling time of the control scheme. In [13,15,18], to estimate the grid phase angle, a zero-state vector is applied to the inverter, and then, the grid angle is derived from the measured currents. However, this technique causes a severe overcurrent in the system. Other methods in [7,10] utilize the rectifier operation mode to extract the grid information before starting the controller in the L-filtered inverter. In the case of an LCL-filtered inverter, the start-up procedure presented in [11] exploits small currents flowing through the capacitor branches to effectively estimate the actual grid phase angle.

In this paper, a grid voltage sensorless current control scheme with a frequency adaptation capability is presented for a grid-connected LCL-filtered inverter. For the purpose of stabilizing the LCL-filtered inverter system under adverse grid conditions and grid disturbance, a full-state feedback regulator augmented with multiple control terms in [4,5] is employed. The requirement of reducing the system cost and hardware complexity is further taken into consideration in the design process. For this purpose, the proposed controller utilizes only the grid-side currents and DC-link voltage sensors to control the inverter system. By means of a discrete current-type observer, the system state variables are estimated precisely to accomplish the full-state feedback current controller. The proposed grid voltage estimator based on the integral-resonant current control successfully reconstructs the grid voltages and provides accurate estimates of the grid phase angle and frequency even under severe grid conditions such as the harmonic distortion, grid frequency variation, and sudden phase jump. To guarantee a highly reliable inverter operation of the proposed grid voltage sensorless control scheme, the start-up process presented in [11] is also adopted to avoid the overcurrent problem. The main contributions of this paper are summarized as follows:

- (1) A current control scheme with a frequency adaptation capability is designed for a grid-connected LCL-filtered inverter without using the grid voltage sensing devices.
- (2) The proposed grid voltage estimator reconstructs the distorted grid voltages with high accuracy to ensure the stability of the current-type full-state observer and provide the precise estimates of the grid information, which ensures a stable synchronization process.
- (3) The start-up process is deployed to guarantee a safe start-up of the grid voltage sensorless controller.
- (4) A disturbance rejection performance and system stability are theoretically analyzed based on the frequency response and pole-zero map approaches.

In order to validate the effectiveness and the feasibility of the proposed control scheme, PSIM software-based simulations have been carried out comprehensively under adverse grid conditions including: distorted grid voltages, grid frequency variation, and grid phase angle jump. For practical evidence, the experiments have been also conducted with the same grid conditions by using a three-phase 2 kVA prototype grid-connected inverter system. A fair comparison with the conventional methods is presented to highlight the performance of the proposed control scheme.

2. System Description

Figure 1 represents the circuit topology of a GCI with LCL filter where R_1 , L_1 , R_2 , and L_2 denote the resistances and inductances of the filter in the inverter-side and the grid-side, respectively, and C_f denotes the filter capacitance. This figure also shows the structure of the proposed control algorithm

which comprises a current controller to drive the inverter via the space vector PWM technique, a current-type full-state observer to provide the information on all the system state variables, and a grid voltage estimator to reconstruct the actual grid voltages. Since a grid voltage estimator extracts the grid line voltages without the voltage measurement, it realizes the sensorless control scheme of the inverter. Obviously, the proposed control scheme requires only three sensing devices to operate the inverter system, which are one DC-link voltage sensor and two grid current sensors. It is worth noting that the superscript in each variable denotes the reference frame. In this paper, the superscripts ‘a’, ‘b’, ‘c’ denote the variables in the natural reference frame, ‘α’, ‘β’ denote those in the stationary frame, and ‘d’, ‘q’ denote those in the SRF. Moreover, the variables with hat ‘^’ denote the estimated quantities provided from the respective observers.

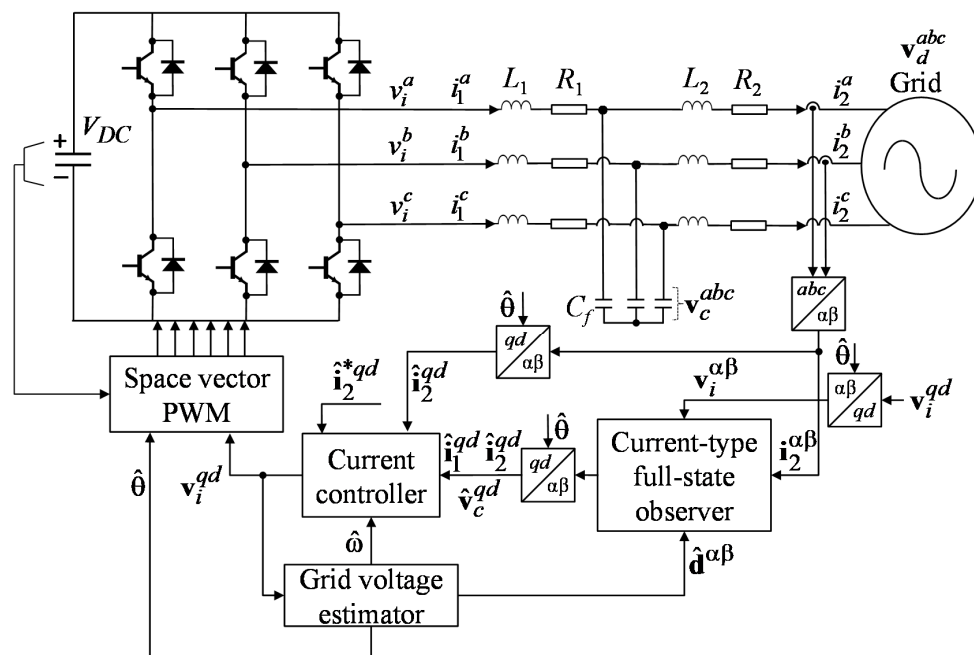


Figure 1. Power circuit of a three-phase grid-connected inverter with inductive–capacitive–inductive (LCL) filter.

A mathematical model of the three-phase LCL-filtered inverter system in the natural reference frame is found in [4,5], in which the LCL-filtered VSI model is expressed for phase-*a* as:

$$\frac{d}{dt} i_1^a(t) = -\frac{R_1}{L_1} i_1^a(t) + \frac{1}{L_1} v_i^a(t) - \frac{1}{L_1} v_c^a(t) \tag{1}$$

$$\frac{d}{dt} i_2^a(t) = -\frac{R_2}{L_2} i_2^a(t) + \frac{1}{L_2} v_c^a(t) - \frac{1}{L_2} v_d^a(t) \tag{2}$$

$$\frac{d}{dt} v_c^a(t) = \frac{1}{C_f} i_1^a(t) - \frac{1}{C_f} i_2^a(t) \tag{3}$$

where i_1 , i_2 , and v_c denote the inverter-side current, the grid-side current, and the capacitor voltage, respectively, v_i is the inverter voltage, and v_d denotes the grid voltage. Similar equations are applied for phases $-b$ and $-c$.

3. Proposed Grid Voltage Sensorless Frequency Adaptive Current Control

In this section, the proposed frequency adaptive sensorless current control scheme is described, in which the current control algorithm and the current-type full-state observer for estimating the system state variables are briefly presented owing to the detailed development in the previous works [4,5].

Alternatively, the discussion is focused on a disturbance rejection performance and stability analysis of the deployed current controller. For the purpose of realizing the grid voltage sensorless control scheme, the current control-based grid voltage estimator developed for the LCL-filtered inverter is discussed. The start-up procedure is also presented to ensure the reliability of the proposed sensorless control scheme.

3.1. Frequency Adaptive Current Controller and Discrete-Time Current-Type Full-State Observer

The current controller is depicted in Figure 2, which solves the inherent resonance phenomenon of the LCL-filtered inverter by a full-state feedback regulator in the SRF. For full-state feedback, the system state variables constitute the system state vector as $\mathbf{x} = [i_2^q \ i_2^d \ i_1^q \ i_1^d \ v_c^q \ v_c^d]^T$. Since the additional sensing devices except for the grid-side currents and DC-link voltage sensors are not used in the proposed system, the current-type full-state observer is adopted to provide precisely the information on the remaining state variables as the inverter-side currents and capacitor voltages.

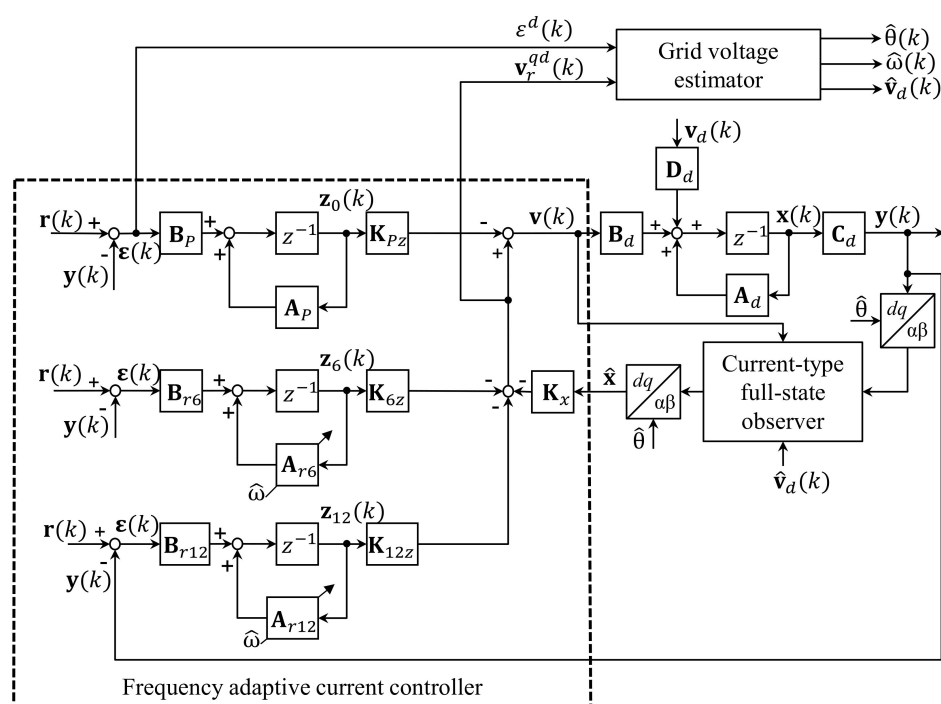


Figure 2. Block diagram of the proposed current controller.

To achieve other essential control objectives such as the asymptotical reference tracking of the grid-injected currents with the immunity to the negative effects from the distorted grid environment, the error between the reference and measured grid-side currents are fed to other control terms such as the integral and resonant terms tuned at interested harmonics, respectively. The frequency information in the resonant terms is updated with online by the estimated grid frequency to maintain the performance of the current controller under grid frequency variation as shown in Figure 2. The control block diagram shows that the control terms are presented in the state-space form and then combined with the full-state feedback regulator. Proper feedback gain sets of K_x , K_{Pz} , K_{6z} , and K_{12z} are chosen systematically by the linear quadratic regulator (LQR) approach. Except for the fact that the grid voltage estimations are used instead of direct measurements, the design process for gain selections of the current controller and the full-state observer are similar to the previous works.

It is worth noting that the grid voltage estimator has a direct influence on both the effectiveness and performance of the grid-connected inverter operation. Firstly, the full-state observer needs the same input quantities as the actual plant, which are the inverter and grid voltages, to maintain the stability and high accuracy of the state estimations. Since the space vector modulation technique

ensures a good match between the inverter voltages and outputs of the current controller, it is valid to directly feed the current controller outputs to the observer. In the grid voltage sensorless control approach, the measurement of the actual grid voltages for feeding back to the state observer is not available. Thus, the estimated grid voltages by the proposed scheme should be quite closed with the actual quantities. Secondly, the capability of resonant controllers to compensate the harmonic distortion from the grid is easily degraded as the frequency in resonant controllers is mismatched with that of the real grid. As a result, the estimated grid frequency should be highly accurate and track the actual value fast even when there exists a frequency variation occurring in the main grid.

As shown in Figure 2, the estimated grid information including the grid voltages, grid phase angle, and frequency is obtained from the proposed grid voltage estimator, which uses the current controller output as the inputs. The detailed development on the proposed grid voltage estimator is presented in the next section.

3.2. Grid Voltage Estimator Based on the Integral-Resonant Current Controller

In this section, a current controller-based grid voltage estimator is presented to effectively estimate the information on three-phase grid voltages such as the grid voltage magnitude, phase angle, and frequency. Inspired by the research work [13], the output of integral control term in the *d*-axis is utilized to obtain the phase angle error signal. By means of the observer concept in modern control, the phase angle error signal is used to drive an observer to estimate the phase angle and frequency of the actual grid voltage.

The continuous-time representation of the LCL-filtered VSI expressed in the natural reference frame in (1)–(3) can be transformed to the rotating estimation frame with the estimated grid phase angle as $\hat{\theta}$, and be expressed in a state-space model as:

$$\dot{\mathbf{x}}(t) = \mathbf{A}\mathbf{x}(t) + \mathbf{B}\mathbf{v}(t) + \mathbf{D}\mathbf{v}_d(t) \tag{4}$$

$$\mathbf{y}(t) = \mathbf{C}\mathbf{x}(t) \tag{5}$$

where $\mathbf{x} = [i_2^q \ i_2^d \ i_1^q \ i_1^d \ v_c^q \ v_c^d]^T$ is the system state vector, $\mathbf{v} = [v_i^q \ v_i^d]^T$ is the system input vector, $\mathbf{v}_d = [V_p \cos(\tilde{\theta}) \ V_p \sin(\tilde{\theta})]^T$ is the grid voltage vector, $\tilde{\theta} = \theta - \hat{\theta}$ is the difference between the actual grid voltage phase angle θ and the estimated one $\hat{\theta}$, and V_p is the magnitude of the grid voltage. The system matrices \mathbf{A} , \mathbf{B} , \mathbf{C} , and \mathbf{D} are presented as:

$$\mathbf{A} = \begin{bmatrix} -R_2/L_2 & -\omega & 0 & 0 & 1/L_2 & 0 \\ \omega & -R_2/L_2 & 0 & 0 & 0 & 1/L_2 \\ 0 & 0 & -R_1/L_1 & -\omega & -1/L_1 & 0 \\ 0 & 0 & \omega & -R_1/L_1 & 0 & -1/L_1 \\ -1/C_f & 0 & 1/C_f & 0 & 0 & -\omega \\ 0 & -1/C_f & 0 & 1/C_f & \omega & 0 \end{bmatrix}, \mathbf{B} = \begin{bmatrix} 0 & 0 \\ 0 & 0 \\ 1/L_1 & 0 \\ 0 & 1/L_1 \\ 0 & 0 \\ 0 & 0 \end{bmatrix} \tag{6}$$

$$\mathbf{D} = \begin{bmatrix} -1/L_2 & 0 \\ 0 & -1/L_2 \\ 0 & 0 \\ 0 & 0 \\ 0 & 0 \\ 0 & 0 \end{bmatrix}, \mathbf{C} = \begin{bmatrix} 1 & 0 & 0 & 0 & 0 & 0 \\ 0 & 1 & 0 & 0 & 0 & 0 \end{bmatrix}. \tag{7}$$

It is obvious that, once the difference $\tilde{\theta}$ reaches to zero, the representation of the LCL-filtered inverter in the SRF is reduced to the model as presented in [4,5].

By defining $X \equiv V_p \sin(\tilde{\theta})$, the value \hat{X} which is an estimate of X can be obtained via an integrator action on the d -axis current error as follows:

$$\frac{d}{dt} \hat{X} = \eta(i_2^{d*} - i_2^d) \tag{8}$$

where η is the estimation gain. To estimate the grid voltage phase angle and frequency from (8), an observer can be established based on the model as below:

$$\frac{d}{dt} \theta = \omega \tag{9}$$

$$\frac{d}{dt} \omega = 0. \tag{10}$$

From (9) and (10), a full-state observer is constructed as:

$$\frac{d}{dt} \begin{bmatrix} \hat{\theta} \\ \hat{\omega} \end{bmatrix} = \begin{bmatrix} 0 & 1 \\ 0 & 0 \end{bmatrix} \begin{bmatrix} \hat{\theta} \\ \hat{\omega} \end{bmatrix} + \begin{bmatrix} \alpha_1 \\ \alpha_2 \end{bmatrix} \tilde{\theta} \tag{11}$$

where $\tilde{\theta} \approx \sin(\tilde{\theta}) = \frac{\hat{X}}{V_p}$.

Instead of using a similar concept which employs the q -axis voltage to estimate the grid voltage magnitude as presented in [13], the grid voltage magnitude is replaced by the q -axis capacitor voltage estimated from the current-type full-state observer in this study with the assumption that the voltage drop across a small size grid-side inductor is negligible. As a result, the grid phase error is obtained as:

$$\tilde{\theta} \approx \sin(\tilde{\theta}) = \frac{\hat{X}}{V_p} = \frac{\hat{X}}{v_c^q}. \tag{12}$$

For a digital implementation, the observer in (11) is discretized by a simple forward Euler method with the sampling time T_s . The observer gains α_1 and α_2 in (11) are chosen in order that the observer poles are located inside the unit circle. In this study, the gains are selected as $\alpha_1 = 0.952$ and $\alpha_2 = 9.51$.

As the grid phase angle and frequency well converge to the actual quantities, the fundamental grid voltages in the stationary frame are obtained from the estimated quantities to feed them into the current-type full-state observer as follows:

$$\hat{v}_{d1}^\alpha = \hat{v}_c^q \cos(\hat{\theta}) \tag{13}$$

$$\hat{v}_{d1}^\beta = \hat{v}_c^q \sin(\hat{\theta}). \tag{14}$$

Generally, the main grid is often contaminated with distorted harmonics although the harmonic magnitudes are significantly smaller than the fundamental component. In the current-type full-state observer designed in [4], the actual grid voltages are required to be fed into the observer structure for ensuring a good performance of the state estimation. To successfully eliminate the grid voltage sensor while still maintaining the stability of the state observer, the estimation for the distorted harmonics in the main grid is further investigated.

It is recognized that in the steady-state condition, the current controller has the main role to diminish the error between the reference and grid-side current. Hence, the output signals of current controller must contain the same harmonic components as distorted grid voltages. Furthermore, because it is valid to assume that the LCL filter impedances generate a trivial voltage drop and phase shift between inverter and grid voltages, it is reasonable to combine the outputs of the resonant control terms into the estimated fundamental grid component in (13) and (14) to fully reconstruct the estimated grid voltages.

In summary, the detailed block diagram of the proposed grid voltage estimator is represented in Figure 3, in which the outputs of the resonant control terms are transformed from the SRF to the stationary frame and added to the fundamental components to form the estimated grid voltages.

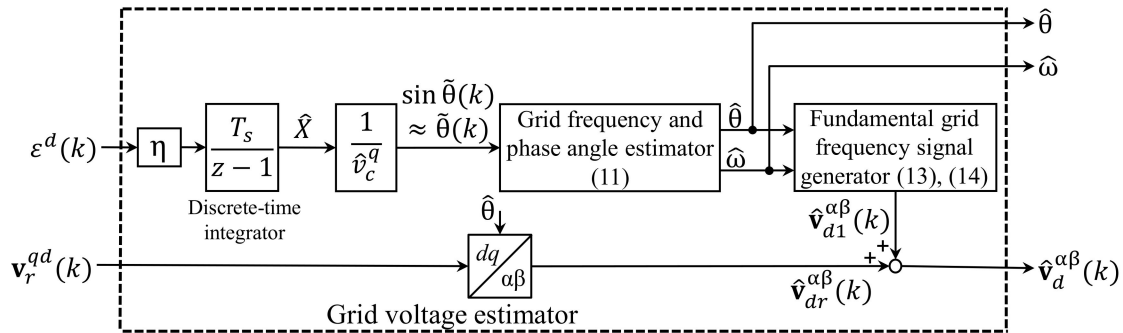


Figure 3. Block diagram of the proposed estimator for the grid voltage, phase angle, and frequency.

3.3. Disturbance Rejection Performance and Stability Analysis

In this subsection, the capabilities of the current controller to track the reference and to reject the disturbances from a distorted grid environment are assessed by the Bode plot of the closed-loop transfer function which relates the output grid current i_2^q to its reference i_2^{q*} , and the transfer function from the disturbance d^q to the system output i_2^q . These two transfer functions are expressed as follows:

$$TF_{cl}(z) = \frac{i_2^q(z)}{i_2^{q*}(z)} \tag{15}$$

$$TF_{dy}(z) = \frac{i_2^q(z)}{v_d^q(z)}. \tag{16}$$

In addition, the eigenvalue plot of the closed-loop system is also presented to verify the stability of the control scheme.

The transfer functions $TF_{cl}(z)$ and $TF_{dy}(z)$ are derived from the entire system model which is obtained by augmenting the integral and resonant control terms into the system model, as follows:

$$\mathbf{x}_e(k+1) = \mathbf{A}_e \mathbf{x}_e(k) + \mathbf{B}_e \mathbf{u}(k) + \mathbf{D}_e \mathbf{v}_d(k) + \mathbf{B}_{re} \mathbf{r}(k) \tag{17}$$

$$\mathbf{y}(k) = \mathbf{C}_e \mathbf{x}_e(k) \tag{18}$$

$$\mathbf{u}(k) = -\mathbf{K} \mathbf{x}_e(k) \tag{19}$$

where $\mathbf{x}_e = [\mathbf{x}^T \mid \mathbf{z}_0^T \mid \mathbf{z}_6^T \mid \mathbf{z}_{12}^T]^T$, $\mathbf{A}_e = \begin{bmatrix} \mathbf{A}_d & \mathbf{0}_{6 \times 2} & \mathbf{0}_{6 \times 4} & \mathbf{0}_{6 \times 4} \\ -\mathbf{B}_p \mathbf{C}_d & \mathbf{A}_p & \mathbf{0}_{2 \times 4} & \mathbf{0}_{2 \times 4} \\ -\mathbf{B}_{r6} \mathbf{C}_d & \mathbf{0}_{4 \times 2} & \mathbf{A}_{r6} & \mathbf{0}_{4 \times 4} \\ -\mathbf{B}_{r12} \mathbf{C}_d & \mathbf{0}_{4 \times 2} & \mathbf{0}_{4 \times 4} & \mathbf{A}_{r12} \end{bmatrix}$, $\mathbf{B}_e = \begin{bmatrix} \mathbf{B}_d \\ \mathbf{0}_{2 \times 2} \\ \mathbf{0}_{4 \times 2} \\ \mathbf{0}_{4 \times 2} \end{bmatrix}$, $\mathbf{D}_e = \begin{bmatrix} \mathbf{D}_d \\ \mathbf{0}_{2 \times 2} \\ \mathbf{0}_{4 \times 2} \\ \mathbf{0}_{4 \times 2} \end{bmatrix}$, $\mathbf{B}_{re} = \begin{bmatrix} \mathbf{0}_{6 \times 2} \\ \mathbf{B}_p \\ \mathbf{B}_{r6} \\ \mathbf{B}_{r12} \end{bmatrix}$

$\mathbf{C}_e = [\mathbf{C}_d \mid \mathbf{0}_{2 \times 2} \mid \mathbf{0}_{2 \times 4} \mid \mathbf{0}_{2 \times 4}]$, $\mathbf{r}(k) = [i_2^{q*}(k) \quad i_2^{d*}(k)]^T$, $\mathbf{K} = [\mathbf{K}_x \mid \mathbf{K}_{pz} \mid \mathbf{K}_{6z} \mid \mathbf{K}_{12z}]$. The matrices \mathbf{A}_d , \mathbf{B}_d , \mathbf{D}_d , and \mathbf{C}_d are the discretized counterparts for the system matrices \mathbf{A} , \mathbf{B} , \mathbf{C} , and \mathbf{D} by the zero-order hold method. The control matrices are derived as:

$$\mathbf{A}_p = \mathbf{I}_{2 \times 2}, \mathbf{B}_p = T_s \times \mathbf{I}_{2 \times 2}, \mathbf{z}_0(k) = [z_0^q(k) \quad z_0^d(k)]^T, \mathbf{z}_n = [\delta_{1n}^q \quad \delta_{2n}^q \quad \delta_{1n}^d \quad \delta_{2n}^d]^T$$

$$\mathbf{A}_{rn} = \begin{bmatrix} 2 \cos(n\hat{\omega}T_s) & 1 \\ -1 & 0 \end{bmatrix}, \mathbf{B}_{rn} = \begin{bmatrix} \cos(n\hat{\omega}T_s) \\ -1 \end{bmatrix} \text{ for } n = 6, 12$$

where $\mathbf{I}_{m \times p}$ and $\mathbf{0}_{m \times p}$ denote the identity and zero matrices with appropriate dimension. The detailed development is presented in the previous works [4,5]. As a result, the closed-loop transfer function of the entire system in (17)–(19) is deduced as:

$$TF_{cl}(z) = \frac{i_2^q(z)}{i_2^{q*}(z)} = \mathbf{C}_e(z\mathbf{I} - \mathbf{A}_e)^{-1}\mathbf{B}_{re} \tag{20}$$

$$TF_{yd}(z) = \frac{i_2^q(z)}{v_d^q(z)} = \mathbf{C}_e(z\mathbf{I} - \mathbf{A}_e)^{-1}\mathbf{D}_e. \tag{21}$$

The Bode diagram of the closed-loop transfer function $TF_{cl}(z)$ is represented in Figure 4a. Obviously, the distorted harmonics at 360 Hz and 720 Hz corresponding to 6th and 12th orders, respectively, are well compensated with significantly low gains, whereas the controller maintains a good reference tracking performance at the fundamental frequency with the unity gain magnitude. The Bode diagram of the transfer function $TF_{yd}(z)$ is shown in Figure 4b to verify the disturbance rejection performance of the inverter system. From the frequency response analysis of the system which is subject to a disturbance from the main grid, the greatly reduced magnitudes at the harmonic frequencies in the Bode plot represent an improvement in the grid harmonic rejection capability. Hence, introducing specified resonant control terms into the current controller considerably improves the grid-injected currents while still maintaining the reference tracking objective. The analysis results by the frequency responses validate the performance of the presented current controller well.

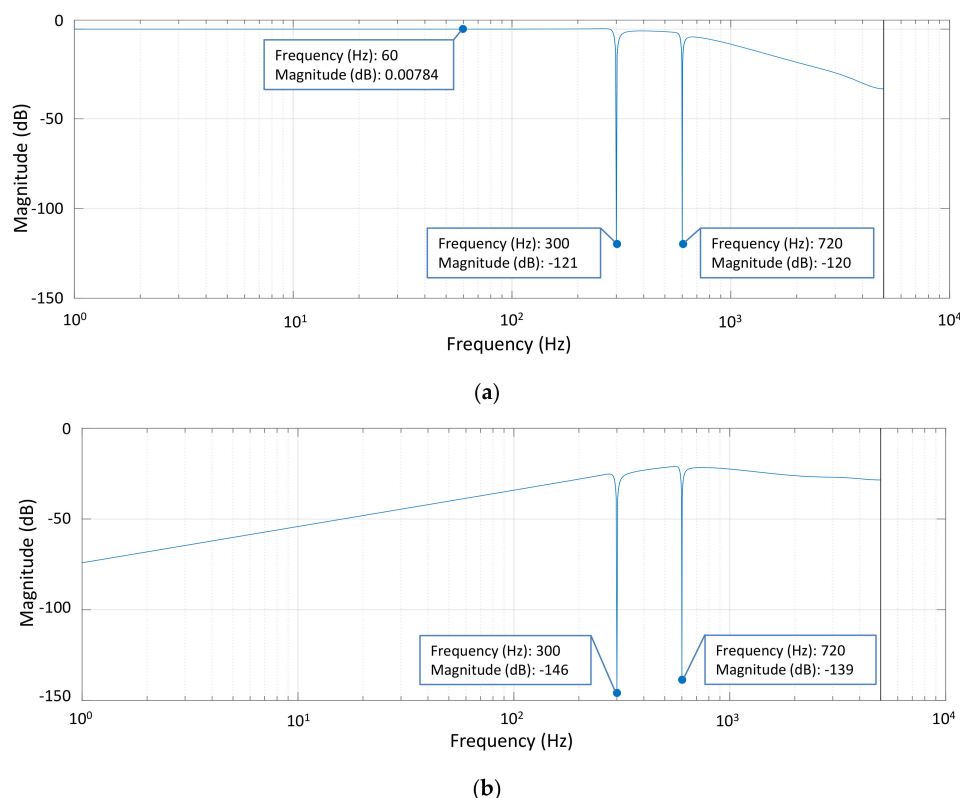


Figure 4. Frequency responses of the closed-loop transfer functions. (a) $TF_{cl}(z)$; (b) $TF_{yd}(z)$.

To investigate the system stability further, the eigenvalue plot of the current controller is presented for a different grid frequency in Figure 5. By means of the LQR approach to select the optimal feedback gain set in a systematical way and the frequency adaptability, the closed-loop poles are maintained in the stable region even when the grid frequency varies in a wide range from 50 Hz to 60 Hz.

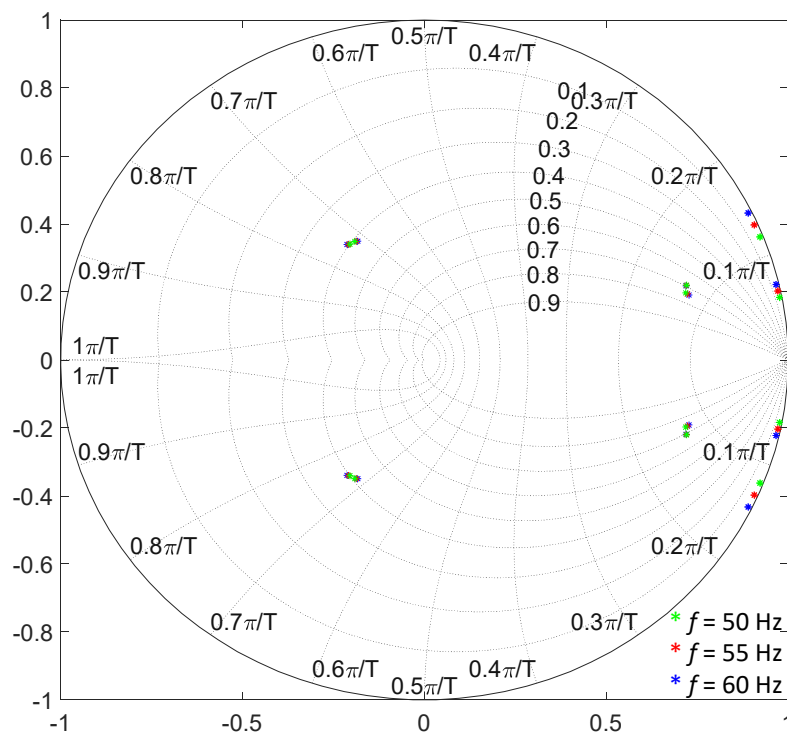


Figure 5. Eigenvalue map of the integral-resonant current controller for different grid frequency.

3.4. Start-Up Procedure

Since the information of the grid voltages is not obtained from the sensing devices in the proposed sensorless control scheme, a start-up procedure should be applied to ensure a rapid synchronization and system stabilization during the start-up period. To avoid the severe overshoot currents and slow convergence of the proposed grid voltage estimator, the actual grid phase angle should be known before the start of the control algorithm. Therefore, the initial grid phase angle detection based on the measured currents when disabling the inverter operation as proposed in [11] is employed in this study.

Assuming that the DC-link input capacitor is fully charged, no current flows back into the inverter from the main grid. However, there are small currents going through the filter capacitor branches and these currents can be detected by the grid-side current sensors. Since the phase angle of the detected currents are different by 90° with respect to the grid voltages, these measured currents can be used effectively to determine the initial grid phase angle. Other information of the grid frequency and grid voltage magnitude are chosen by the best prior system knowledge. The first guess of the grid voltage magnitude is also used to suppress the current overshoot by means of a grid-voltage feedforward concept [19].

4. Simulation Results

To evaluate the performance of the proposed grid voltage sensorless current control scheme presented in this paper, PSIM software-based simulations were carried out using the LCL-filtered GCI as shown in Figure 1, with the system parameters listed in Table 1. It is also worth noting that the actual grid voltages are measured by voltage sensors only for comparison purposes, without using in the control algorithm.

Table 1. System parameters of a grid-connected inverter.

Parameters	Value	Units
DC-link voltage	420	V
Resistance (load bank)	24	Ω
Filter resistance	0.5	Ω
Filter capacitor	4.5	μF
Inverter-side filter inductance	1.7	mH
Grid-side filter inductance	1.7	mH
Grid voltage (line-to line rms)	220	V
Grid frequency	50–60	Hz
Switching frequency/Sampling frequency	10	KHz

In order to simulate the worst operation condition happening in the main grid, the proposed current control scheme is verified under distorted grid voltages containing the harmonic components in the orders of 5th, 7th, 11th, and 13th with 5% magnitude of the fundamental grid voltage as represented in Figure 6a. The fast Fourier transform (FFT) result of phase-*a* voltage is also shown in Figure 6b to clearly visualize the magnitude of distorted harmonics, in which the total harmonic distortion (THD) is 9.99%.

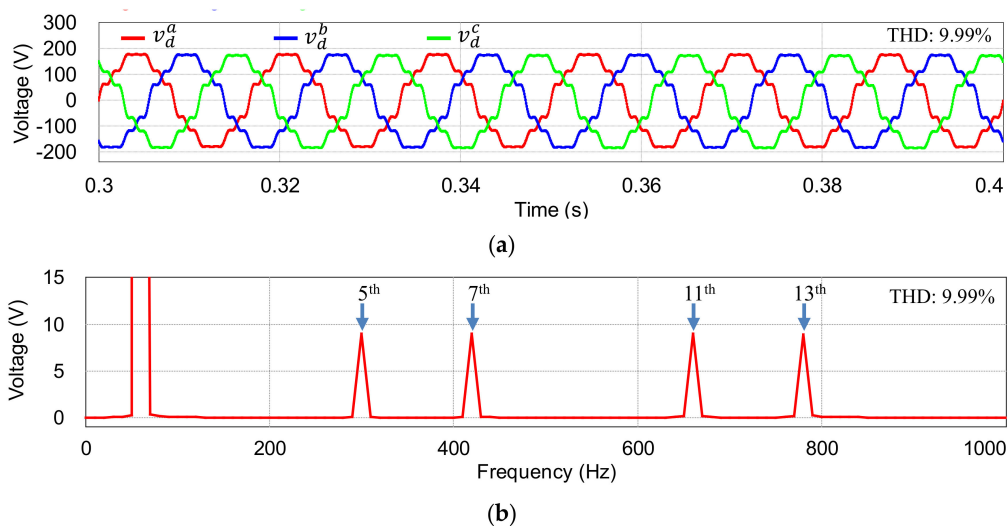


Figure 6. Distorted three-phase grid voltages. (a) Three-phase voltages; (b) fast Fourier transform (FFT) result of phase-*a* voltage.

Figure 7 shows the simulation results of three-phase grid-side currents at steady-state under the grid condition in Figure 7a. The current injected into the grid is 7 A. The simulation test clearly shows high-quality grid-side currents even in the presence of a severely distorted grid condition with only the THD value of 3.68%, which is compliant with limits specified by the grid interconnection regulation IEEE Std. 1547 [20]. The magnitudes of harmonics are presented more evidently in the FFT result of phase-*a* current as shown in Figure 7b, which illustrates that the current controller well rejects the distorted harmonics from the grid to produce clean output currents.

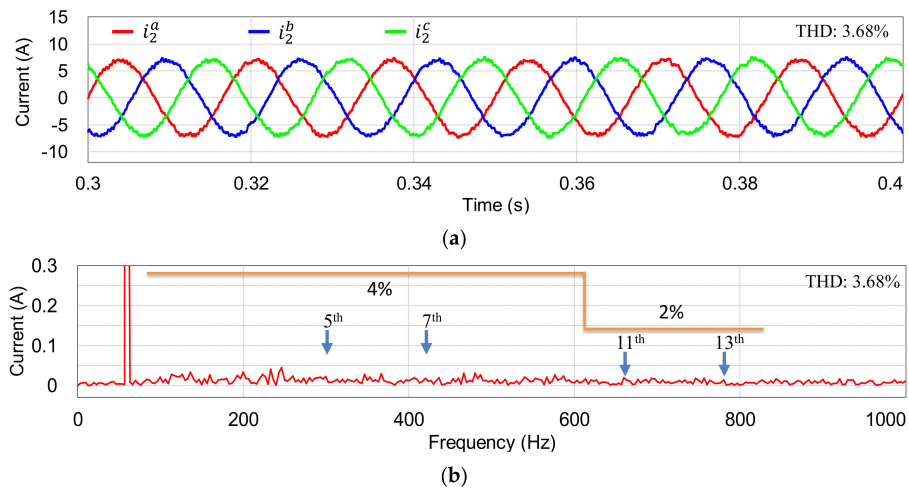


Figure 7. Simulation results for steady-state grid current responses under distorted grid voltage with the proposed controller at 60 Hz. (a) Three-phase grid-side currents; (b) FFT result of phase-*a* current.

In the grid voltage sensorless current control scheme, the control performance such as current overshoot and transient time should be validated because one of the most severe transient responses occurs during the start-up instance. For this purpose, Figure 8a represents the grid current control performance at start-up instance based on the start-up procedure in Section 3.4. As shown in this figure, the current controller starts to control the injected currents at 0.15 s. With the prior information of the actual grid phase angle obtained by the start-up algorithm, and the best guess of the grid frequency and voltage magnitude, the sensorless control can be started smoothly with minimal current overshoot and transient time. The current responses reach the steady state after about 2 grid voltage cycles. Initial transient current overshoot is observed as 8 A. However, it is damped rapidly and it does not trigger the system halt caused by the protection mechanism. To verify the dynamic performance of the current controller, another transient test result is shown in Figure 8b under a step change in the *q*-axis current reference from 4 A to 7 A at 0.25 s. It is obviously shown that the currents quickly track the new reference value without overshoot, which validates the stable and desirable transient response of the proposed control scheme.

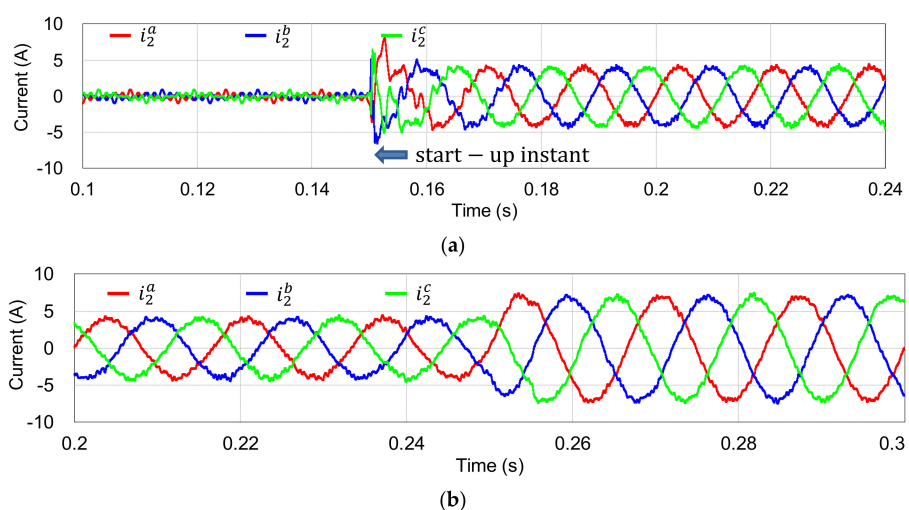


Figure 8. Simulation results for transient grid current responses under distorted grid voltage with the proposed controller at 60 Hz. (a) Start-up process at 0.15 s; (b) Three-phase grid-side currents under step change in *q*-axis current reference at 0.25 s.

Other transient response of the current controller is tested under the frequency of distorted grid varying from 60 Hz to 50 Hz at 0.6 s as depicted in Figure 9a. Since a sudden change in the grid frequency causes the mismatch between the estimated and actual frequency of the grid, the injected phase currents encounter a transient period lasting 38 ms before reaching the steady state at 50 Hz as illustrated in Figure 9b. Figure 9c shows more visibly the estimating performance of the grid frequency by the proposed voltage sensorless scheme in comparing with the actual one f^* , and the output of a moving average filter-based phase locked-loop (MAF-PLL) with the measured grid voltages [21]. Even under abrupt grid frequency variation of f^* , the proposed grid voltage estimator provides a smoother and faster estimated frequency than the MAF-PLL method. Finally, the synchronization behavior of the proposed grid voltage estimation under such an operation condition is validated in view of the estimated grid phase angle. The estimated phase angle is compared to the output of a MAF-PLL in Figure 9d. As expected, the estimated quantity is aligned well with the output of the MAF-PLL and keeps a stable synchronization of the inverter with the main grid even without using the direct grid voltage sensing devices.

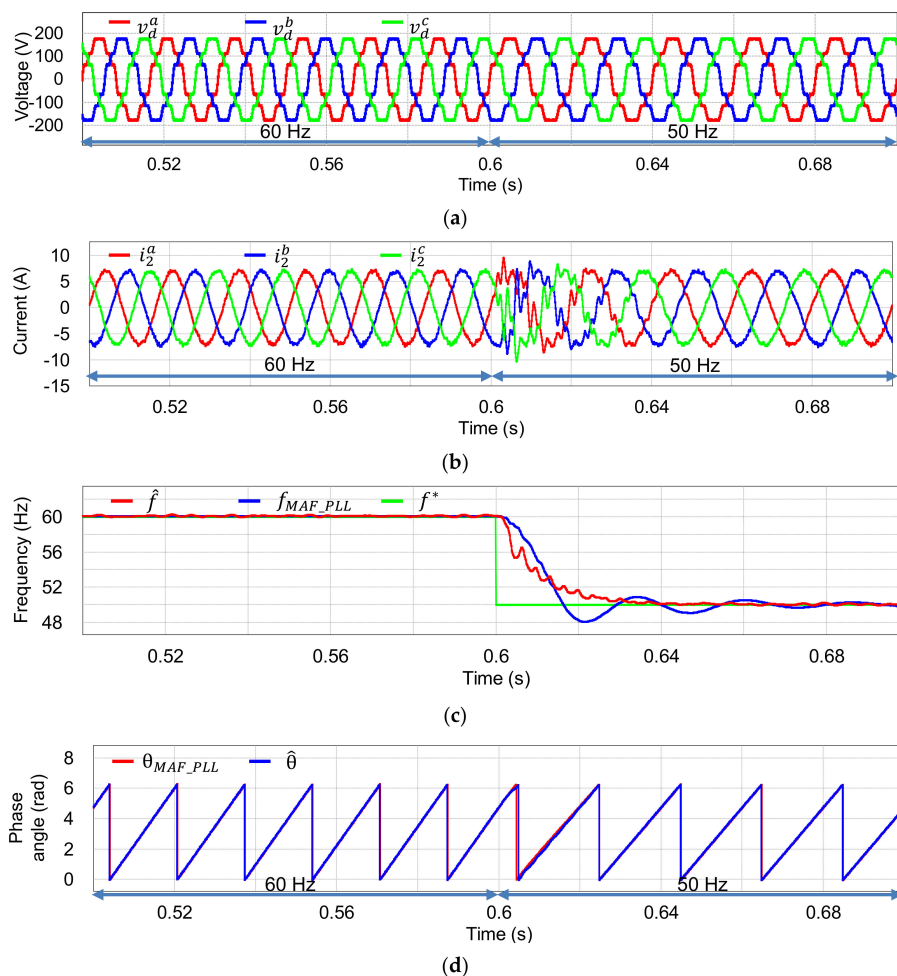


Figure 9. Simulation results of the proposed scheme under grid frequency variation from 60 Hz to 50 Hz at 0.6 s. (a) Three-phase grid voltages; (b) three-phase grid-side currents; (c) estimated frequency by the proposed scheme \hat{f} , the extracted frequency by the moving average filter-based phase locked-loop (MAF-PLL) with measured grid voltages f_{MAF_PLL} , and the actual frequency f^* ; (d) estimated phase angle by the proposed scheme $\hat{\theta}$ and the extracted phase angle from the MAF-PLL with measured grid voltages θ_{MAF_PLL} .

In literature, only a few control schemes are tested under the abrupt phase angle jump which commonly happens during grid line fault events [5,11]. In particular, the controller in [11] using a model-based grid voltage estimator is validated with a phase jump of -60° . The transient time presented in this study is short and satisfactory; however, this paper does not consider the distorted grid harmonics together with the phase jump condition. Another study in [5] represents an adaptive neural network-based grid voltage estimator. Since the phase angle in this paper is still dependent on the performance of the conventional PLL, the transient time lasts 40 ms for the estimated frequency and phase currents reaching steady state.

In this paper, a similar grid condition with a phase angle jump by -30° is considered as a test condition. At the same time, the grid frequency is changed from 60 Hz to 50 Hz at 0.6 s as presented in Figure 10a. The distortion level in the grid is maintained as the previous tests. Obviously, even with the sensor-based control scheme, the grid phase current response shows a serious transient time and the steady-state will be reached only after the grid phase angle and frequency converge with the actual quantities. The transient time mostly depends on the dynamic of the synchronization technique if the current controller ensures a sufficiently fast response. Figure 10b shows the transient performance of the proposed scheme, in which the grid-side phase currents have very short transient time of only 20 ms, and the overshoot current is damped fast. Clearly, the fast response of the current controller is facilitated by the high accuracy of the estimated grid frequency and phase angle as demonstrated in Figure 10c,d, respectively. In spite of using the direct grid voltage measurements, the detected grid frequency from the MAF-PLL shows larger overshoot and longer settling time as plotted in Figure 10c, which highlights a superior response of the grid voltage estimator.

To further verify the robustness of the proposed current controller against system parametric uncertainties, more simulations are conducted with the uncertainties of the filter capacitors and the weak grid condition.

Figure 11 represents the grid current responses under distorted grid and uncertainty in system parameters. In particular, the filter capacitance value increases to $5.5 \mu\text{F}$ in Figure 11a and decreases to $3.3 \mu\text{F}$ in Figure 11b. Moreover, to consider the parasitic resistance of the filter capacitor caused by the aging effect of the filter capacitors, the resistances R_3 of 2Ω are added to filter capacitors in series in these simulations. As expected, since the proposed current controller designed by the LQR concept has the robustness under system parameter uncertainties, even in these conditions, the three-phase grid currents are still maintained with good performance of the THD at 3.35% and 3.28%, respectively.

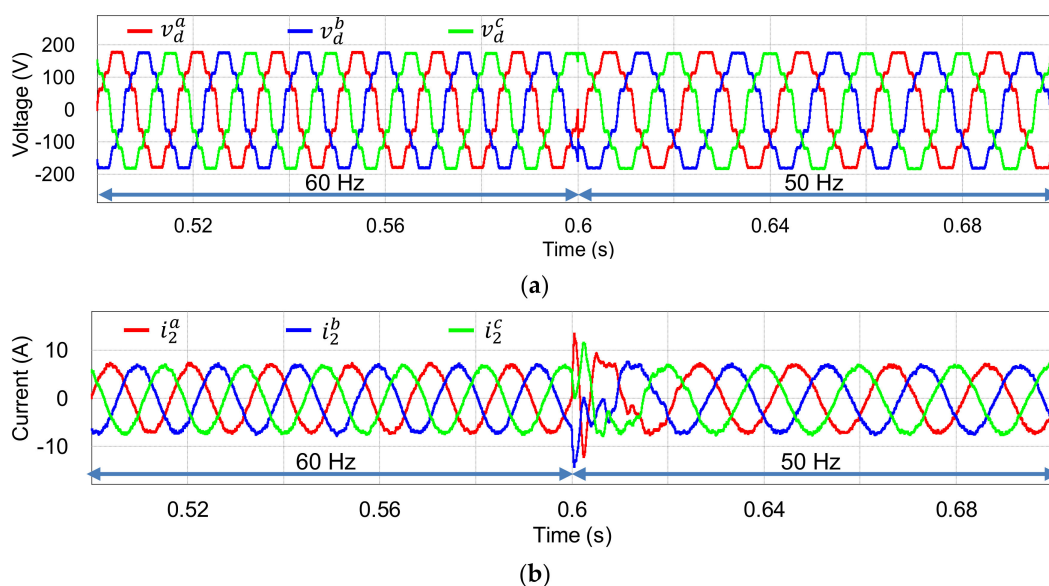


Figure 10. Cont.

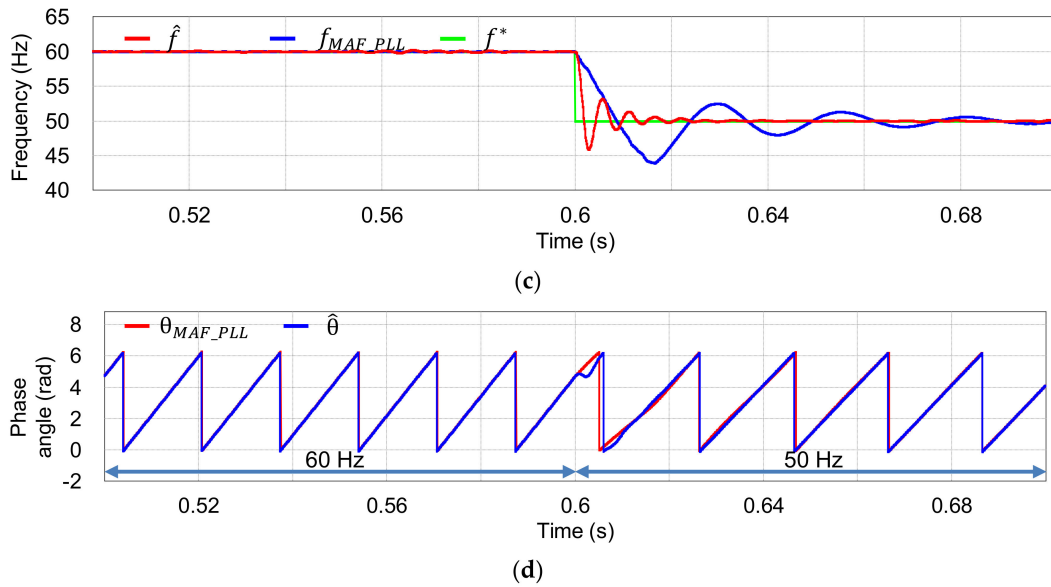


Figure 10. Simulation results of the proposed scheme under grid frequency variation from 60 Hz to 50 Hz and phase jump -30° at 0.6 s. (a) Three-phase grid voltages; (b) three-phase grid-side currents; (c) comparison of the grid frequency between the proposed scheme and the MAF-PLL method; (d) comparison of the grid phase angle between the proposed scheme and the MAF-PLL method.

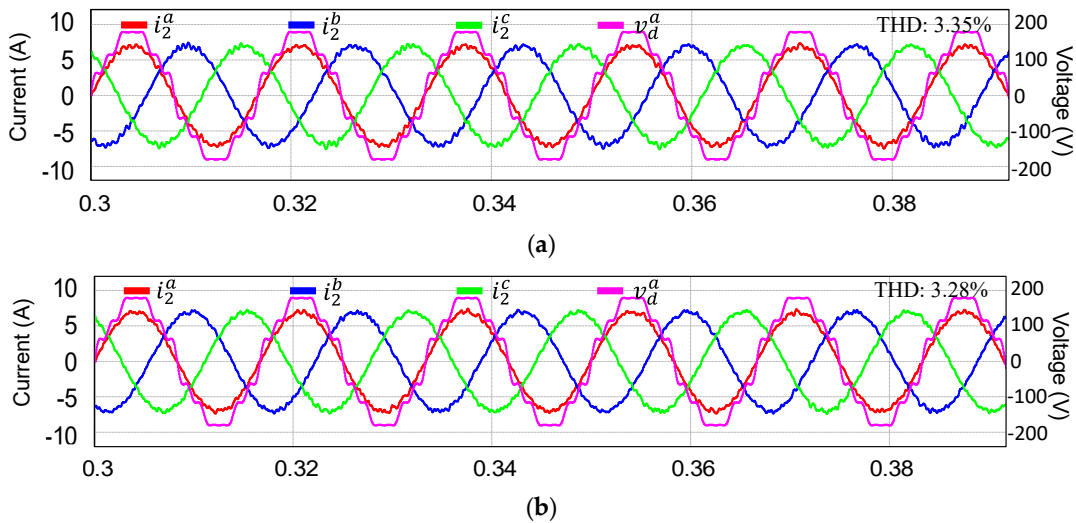


Figure 11. Simulation results for steady-state grid current responses under distorted grid voltage with filter capacitor uncertainties. (a) $C_f = 5.5 \mu F$ and $R_3 = 2 \Omega$; (b) $C_f = 3.5 \mu F$ and $R_3 = 2 \Omega$.

The next test is carried out to consider the weak grid condition, in which additional inductors L_g of 3 mH are connected in series with the grid-side filter inductor L_2 . Figure 12 represents the responses of the proposed grid voltage sensorless control scheme. Obviously, the grid-connected inverter still operates stably with a high quality of injected currents as shown in Figure 12a, and accurate estimated grid voltages as shown in Figure 12b. This simulation demonstrates well the robustness of the proposed current controller under weak grid condition even when there are no grid voltage sensors installed in the system.

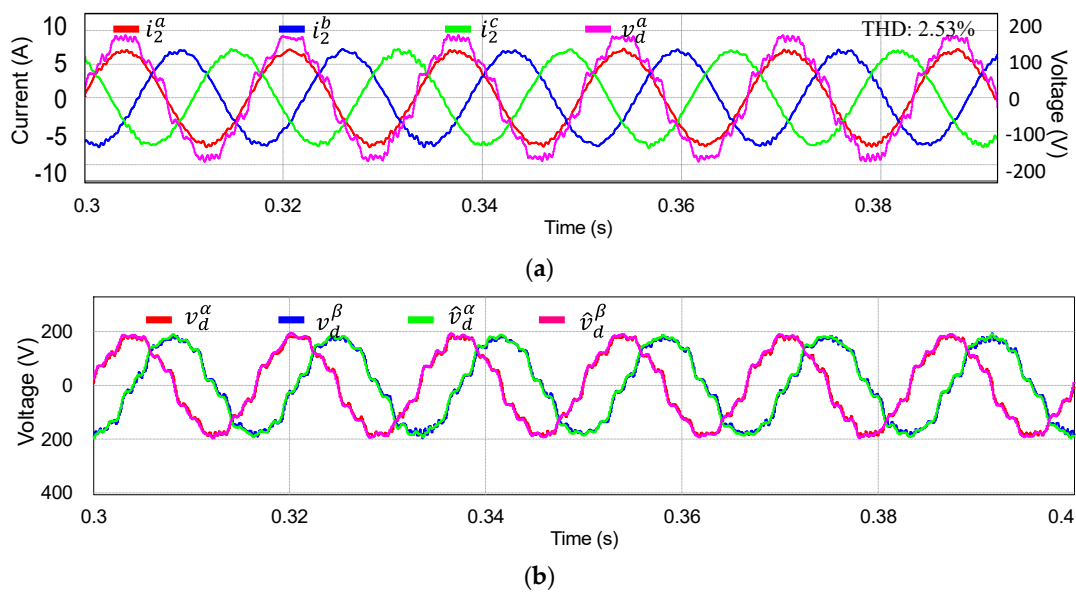


Figure 12. Simulation results for steady-state grid current responses under distorted weak grid voltage with grid inductor L_g of 3 mH. (a) Three-phase grid-side currents; (b) measured and estimated grid voltages in the stationary reference frame.

In summary, the presented simulation results prove the capability of the proposed voltage sensorless current controller to produce high-quality grid-injected currents and a reliable operation under a non-ideal grid environment with the advantage of a lower sensor cost and hardware complexity.

5. Experimental Results

In this section, the feasibility of the proposed grid voltage sensorless control scheme is validated by a lab-based hardware prototype constructing for a three-phase 2 kVA LCL-filtered GCI with the system parameters listed in Table 1. The hardware system configuration and the experimental setup are depicted in Figures 13 and 14, respectively. The overall system was built by a three-phase LCL-filtered inverter controlled by digital signal processor (DSP) TMS320F28335 [22], a magnetic contactor for grid-connecting operation, an alternating current (AC) power source (PACIFIC 320-ASX) to emulate three-phase grid voltages, and sensors to measure the currents and voltages. Similar to the simulation setup, the grid voltage sensors were included in the system for comparison purpose only.

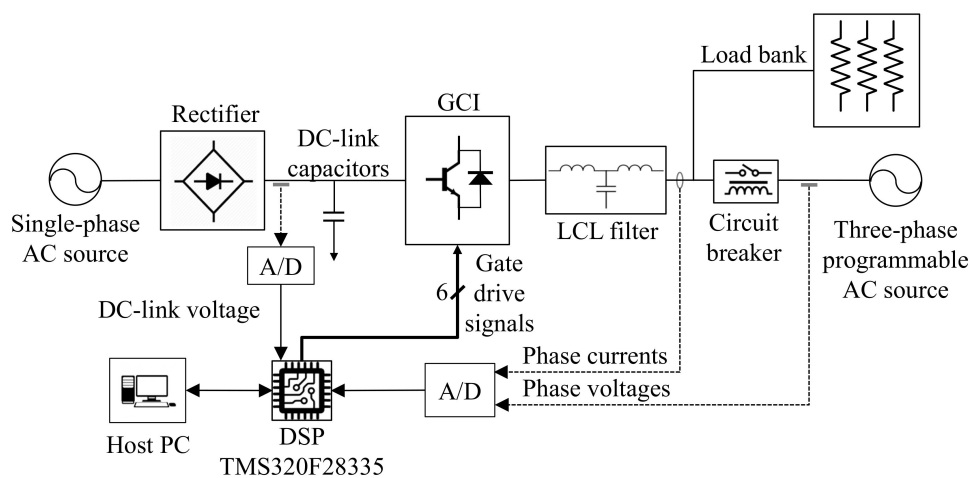


Figure 13. Hardware system configuration.

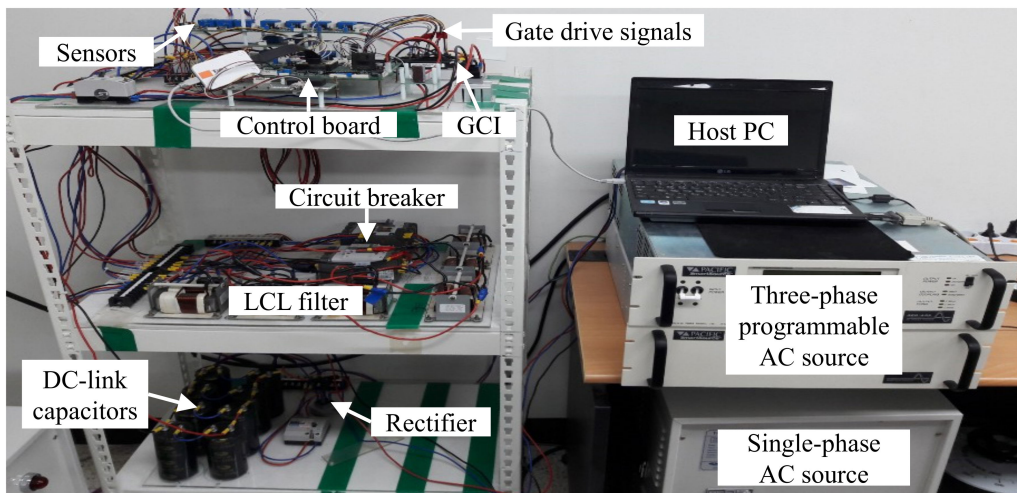


Figure 14. Photograph of experimental setup.

Figure 15a shows distorted grid voltages generated by the AC power source which contain the same distorted harmonic levels as the simulation in Figure 6a. The FFT result of phase-*a* grid voltage clearly presents the fundamental and distorted harmonic grid components in Figure 15b.

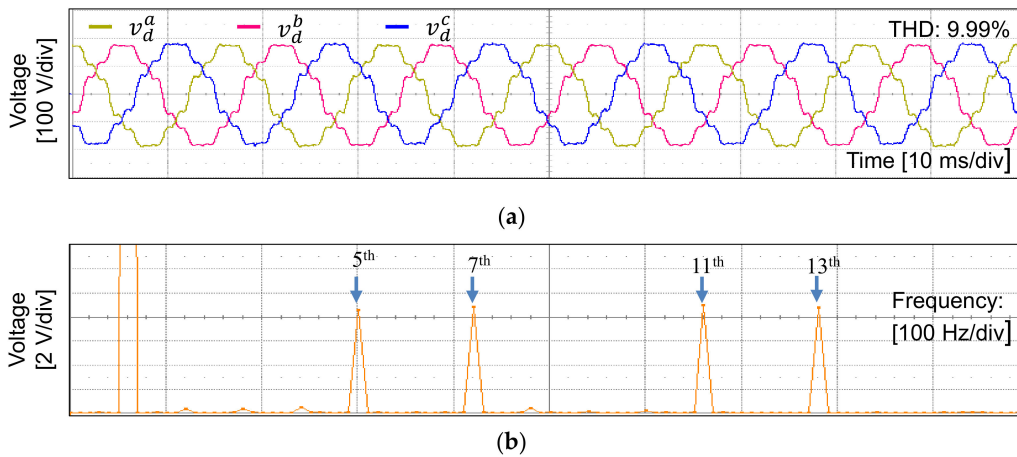


Figure 15. Three-phase distorted grid voltages used for experiments. (a) Three-phase grid voltages; (b) FFT result of phase-*a* voltage.

The experimental results of three-phase grid-side currents at steady-state are shown in Figure 16a together with the measured phase-*a* grid voltage. The considerably sinusoidal waveforms of output currents confirm the effectiveness of the current controller to maintain a good current quality even under the several negative effects from the main grid. Furthermore, phase-*a* current is well aligned with the measured phase-*a* grid voltage, which ensures maximizing the active power injecting to the grid. The FFT result in Figure 16b further shows negligible components of harmonic distortion in phase-*a* injected current. To illustrate the performance of the proposed grid voltage estimator, Figure 16c represents the estimated grid voltages together with the measured one in the stationary frame. A good match between the estimated and measured waveforms experimentally confirms the stability of the proposed grid voltage estimator.

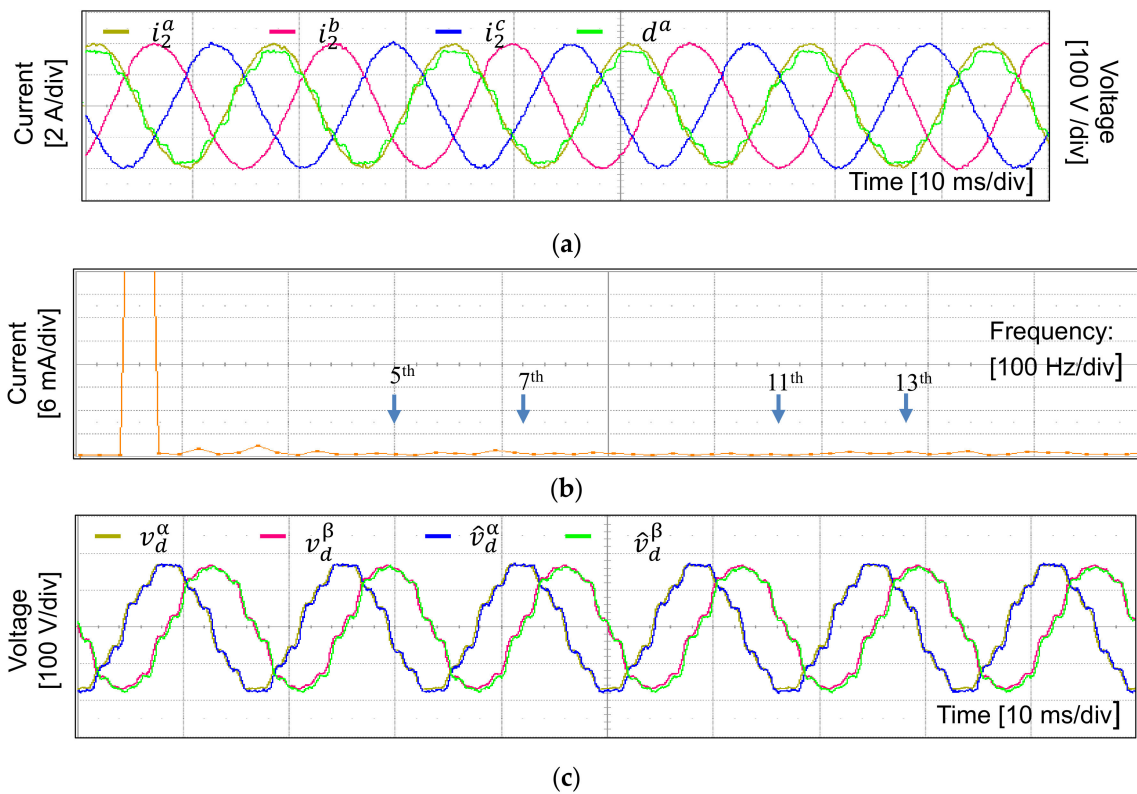


Figure 16. Experimental results for the proposed scheme at steady-state. (a) Three-phase grid currents and measured phase-a voltage; (b) FFT result of phase-a current; (c) measured and estimated stationary grid voltages.

The transient responses of the proposed control scheme are validated by experiments. Figure 17 shows the transient current response of the proposed scheme under the step change in q -axis current reference from 2 A to 4 A, in which the grid-side currents instantly track the new reference without noticeable overshoot. The dynamic performance of the proposed current control shows a good agreement in both the simulation in Figure 8b and the experimental result in Figure 17.

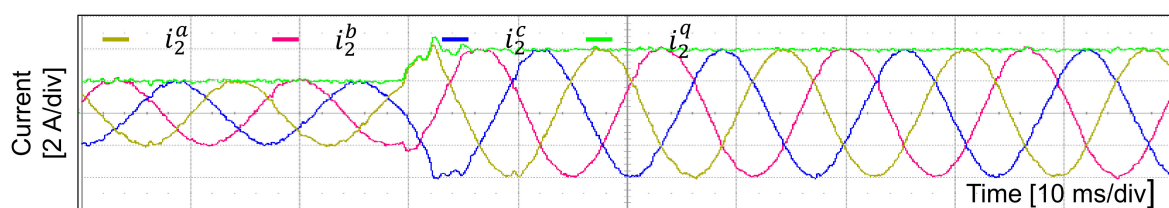


Figure 17. Experimental result for the proposed control scheme under step change in q -axis current reference from 2 A to 4 A: three-phase grid-side current responses.

Another test is conducted to verify the start-up procedure of the sensorless control scheme experimentally. As shown in Figure 18a, the sensorless algorithm is successfully started and the grid phase currents reach steady state rapidly within 30 ms. Similar to the start-up response in the simulation result in Figure 8a, the current overshoot is damped fast and the settling time is short. The estimated grid voltages are represented in Figure 18b with the measured quantities in the stationary frame. It is shown clearly that the estimated values track the measured ones well from the initial time. This demonstrates the effectiveness of the start-up process to provide the correct information of the grid phase angle as well as the fast dynamic characteristics of the grid voltage estimator.

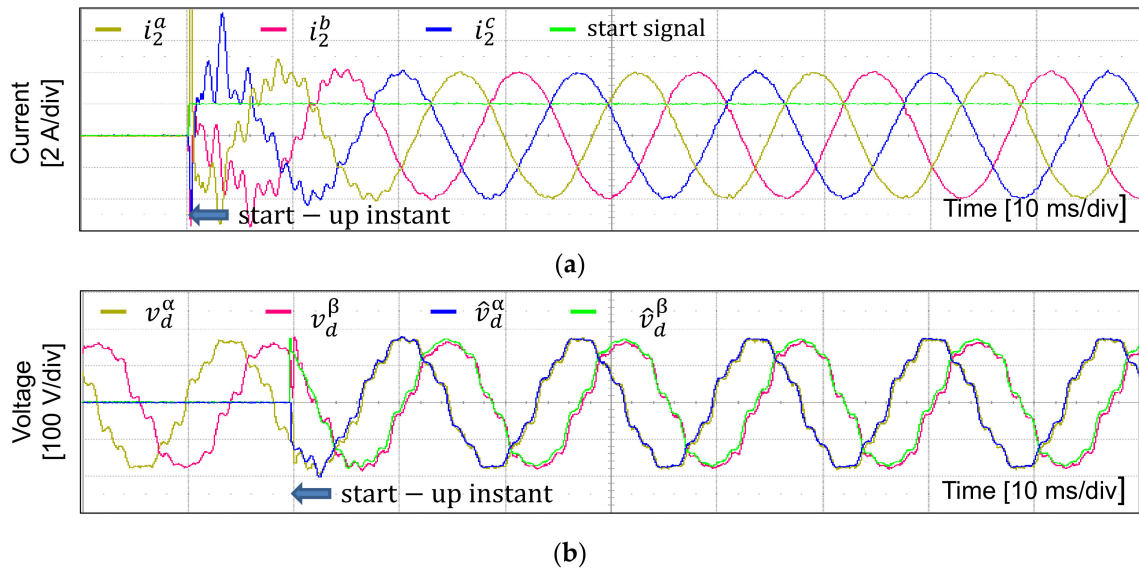


Figure 18. Experimental results for the proposed grid voltage sensorless scheme at start-up instant. (a) Three-phase currents; (b) measured and estimated stationary grid voltages.

The next transient test is conducted with the condition of the grid frequency variation. Figure 19a shows the distorted grid voltages having the frequency jump from 60 Hz to 50 Hz. When the grid frequency is instantly varied, the grid currents are contaminated by the harmonic distortion during around 2 grid cycles before reaching steady-state at the new grid frequency as shown in Figure 19b. The estimated grid frequency is also presented in this figure to clearly explain that the mistuned frequency in the resonant term of the current controller is responsible for the current harmonic distortion. However, as soon as the estimated grid frequency tracks the actual value well, the grid currents are recovered to sinusoidal waveforms. To validate the accuracy of the estimated grid frequency, Figure 19c shows the experimental test result when the actual frequency varies in a small range of 1 Hz. Even for such a small variation, the grid frequency can be detected well with a reasonable fluctuation of only around 0.3 Hz as clearly shown in Figure 19c, restoring the grid currents to being quite sinusoidal.

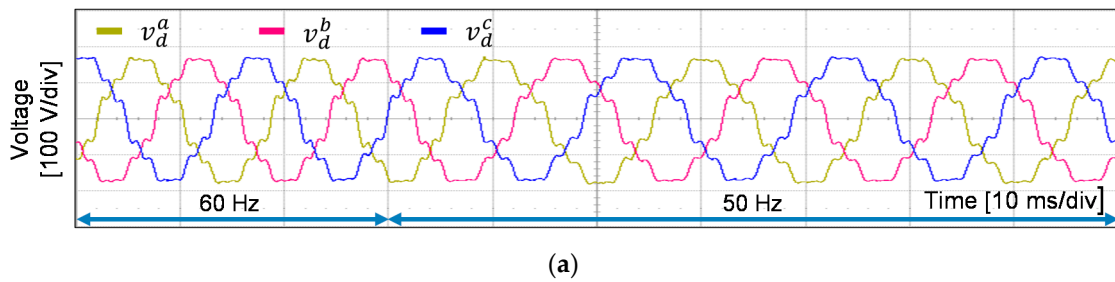


Figure 19. Cont.

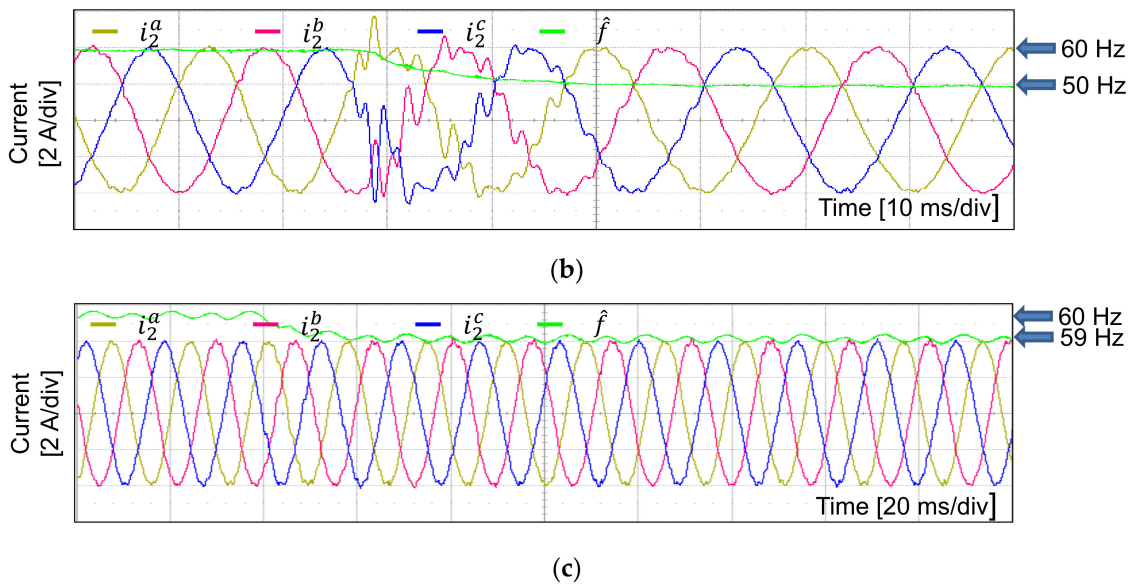


Figure 19. Experimental results for three-phase grid currents under frequency variations with the proposed scheme. (a) Three-phase grid voltages with frequency variation from 60 Hz to 50 Hz; (b) three-phase grid currents and estimated grid frequency under grid frequency variation from 60 Hz to 50 Hz; (c) three-phase grid currents and estimated grid frequency under grid frequency variation from 60 Hz to 59 Hz.

As the final experimental test, the performance of the grid voltage sensorless current controller is validated under both the grid frequency variation and abrupt phase jump condition as shown in Figure 20a, which is exactly the same as the simulation environment in Figure 10a. Remarkably, the grid phase currents and estimated grid frequency reach steady state after only 10 ms in Figure 20b. The grid frequency obtained from the MAF-PLL with the measured grid voltages is also plotted in this figure for the performance comparison. Larger overshoot and longer settling time in the frequency detection by the MAF-PLL may cause a severely degraded transient current response, making it more probable the protection mechanism will be triggered. On the other hand, the proposed current controller effectively handles the grid phase jump condition with fast transient and reduced current overshoot.

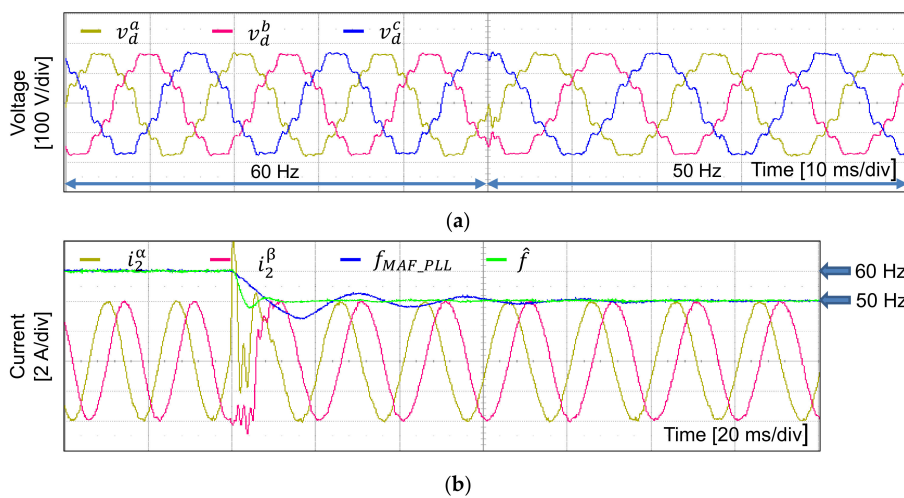


Figure 20. Experimental results of the proposed scheme under grid frequency variation from 60 Hz to 50 Hz and phase jump of -30° . (a) Three-phase grid voltages; (b) stationary grid-side currents, and comparative result of the grid frequency estimations between the proposed control scheme and the MAF-PLL method.

6. Conclusions

In this study, a frequency adaptive current controller for a GCI with an LCL filter has been presented without requiring grid voltage sensing devices. The proposed grid voltage sensorless control scheme is achieved by employing a frequency adaptive integral-resonant current controller and a current control-based grid voltage observer. Although the entire control algorithm is implemented with only the measurements from the grid-side currents and DC-link voltage, the current controller and grid voltage estimator guarantee to maximize the injected active power with high-quality currents into the main grid, which is strictly compliant with the grid interconnection regulations even under several unfavorable grid conditions. The stability and robustness of the current controller has been further investigated by means of the frequency response analysis and eigenvalue plot. To ensure a reliable inverter operation from the beginning, the start-up procedure is also incorporated in this study for a smooth start-up with short settling time. In order to verify the feasibility and effectiveness of the proposed sensorless control scheme, comprehensive simulations and hardware-based experimental tests have been conducted under adverse distorted grid conditions with frequency and phase angle variations. The results obtained confirm a stable and reliable operation of the proposed control method as well as its robustness against the negative effects from the grid even without the grid voltage sensors. A fair comparison to the conventional methods is also presented. It is clearly demonstrated from the comparison results that the grid voltage observer shows a superior performance in terms of very fast and accurate estimation of the grid voltage quantities, grid phase angle, and frequency.

Author Contributions: T.V.T. and K.-H.K. conceived the main concept of the control structure and developed the entire system. T.V.T. carried out the research and analyzed the numerical data with the guidance from Kyeong-Hwa Kim. T.V.T. and K.-H.K. collaborated to prepare the manuscript. All authors have read and agreed to the published version of the manuscript.

Funding: This research was supported by Basic Science Research Program through the National Research Foundation of Korea (NRF) funded by the Ministry of Education (NRF-2019R1A6A1A03032119). This work was supported by the National Research Foundation of Korea (NRF) grant funded by the Korean government (MSIT) (NRF-2020R1F1A1048262).

Conflicts of Interest: The authors declare no conflict of interest.

References

1. Guo, X.; Liu, W.; Zhang, X.; Sun, X.; Lu, Z.; Guerrero, J.M. Flexible control strategy for grid-connected inverter under unbalanced grid faults without PLL. *IEEE Trans. Power Electron.* **2015**, *30*, 1773–1778. [[CrossRef](#)]
2. Chowdhury, V.R.; Kimball, W. Grid voltage estimation and feedback linearization based control of a three phase grid connected inverter under unbalanced grid conditions with LCL Filter. In Proceedings of the 2019 IEEE Energy Conversion Congress and Exposition (ECCE), Baltimore, MD, USA, 29 September–3 October 2019; pp. 2979–2984.
3. Vieira, R.P.; Martins, L.T.; Massing, J.R.; Stefanello, M. Sliding mode controller in a multiloop framework for a grid-connected VSI with LCL filter. *IEEE Trans. Ind. Electron.* **2018**, *65*, 4714–4723. [[CrossRef](#)]
4. Bimarta, R.; Tran, T.V.; Kim, K.-H. Frequency-adaptive current controller design based on LQR state feedback control for a grid-connected inverter under distorted grid. *Energies* **2018**, *11*, 2674. [[CrossRef](#)]
5. Tran, T.V.; Kim, M.; Kim, K.-H. Frequency adaptive current control scheme for grid-connected inverter without grid voltage sensors based on gradient steepest descent method. *Energies* **2019**, *12*, 4266. [[CrossRef](#)]
6. Kennel, R.M.; Linke, M.; Szczupak, P. “Sensorless” control of 4-quadrant-rectifiers for voltage source inverters (VSI). In Proceedings of the PESC’03 2003 IEEE 34th Annual Conference on Power Electronics Specialist, Acapulco, Mexico, 15–19 June 2003; pp. 1057–1062.
7. Zhang, Y.; Wang, Z.; Jiao, J.; Liu, J. Grid-voltage sensorless model predictive control of three-phase PWM rectifier under unbalanced and distorted grid voltages. *IEEE Trans. Power Electron.* **2020**, *35*, 8663–8672. [[CrossRef](#)]
8. Zang, J.; Wang, H.; Zhu, M.; Cai, X. Control implementation of the full-scale wind power converter without grid voltage sensor. In Proceedings of the 2014 International Power Electronics Conference (IPEC-Hiroshima 2014-ECCE ASIA), Hiroshima, Japan, 18–21 May 2014; pp. 1753–1760.

9. Mukherjee, S.; Chowdhury, V.R.; Shamsi, P.; Ferdowsi, M. Grid voltage estimation and current control of a single-phase grid-connected converter without grid voltage sensor. *IEEE Trans. Power Electron.* **2018**, *33*, 4407–4418. [[CrossRef](#)]
10. Rahoui, A.; Bechouche, A.; Seddiki, H.; Abdeslam, D.O. Grid voltages estimation for three-phase PWM rectifiers control without AC voltage sensors. *IEEE Trans. Power Electron.* **2018**, *33*, 859–875. [[CrossRef](#)]
11. Tran, T.V.; Kim, K.-H. Frequency adaptive grid voltage sensorless control of LCL-filtered inverter based on extended model observer. *IEEE Trans. Ind. Electron.* **2020**, *67*, 7560–7573. [[CrossRef](#)]
12. Nazib, A.A.; Holmes, D.G.; McGrath, B.P. High quality grid current control for LCL inverters using self-synchronising inverter side current regulation. In Proceedings of the 2019 10th International Conference on Power Electronics and ECCE Asia (ICPE 2019-ECCE Asia), Busan, Korea, 27–30 May 2019; pp. 2962–2969.
13. Agirman, I.; Blasko, V. A novel control method of a VSC without AC line voltage sensors. *IEEE Trans. Ind. Appl.* **2003**, *39*, 519–524. [[CrossRef](#)]
14. Liserre, M.; Pigazo, A.; Dell’Aquila, A.; Moreno, V.M. An anti-islanding method for single-phase inverters based on a grid voltage sensorless control. *IEEE Trans. Ind. Electron.* **2006**, *53*, 1418–1426. [[CrossRef](#)]
15. Kwon, B.-H.; Youm, J.-H.; Lim, J.-W. A line-voltage-sensorless synchronous rectifier. *IEEE Trans. Power Electron.* **1999**, *14*, 966–972. [[CrossRef](#)]
16. Chatterjee, A.; Mohanty, K.B.; Thakre, K.; Kommukuri, V.S. Grid voltage sensorless control of single phase grid tied inverter for renewable energy systems applications. *Electric Power Compon. Syst.* **2018**, *46*, 1795–1807. [[CrossRef](#)]
17. Ohnishi, T.; Fujii, K. Line voltage sensorless three phase PWM converter by tracking control of operating frequency. In Proceedings of the Power Convers. Conf.—PCC ’97, Nagaoka, Japan, 3–6 August 1997; pp. 247–252.
18. Barrass, P.; Cade, M. PWM rectifier using indirect voltage sensing. *IEE Proc. Electr. Power Appl.* **1991**, *146*, 539–544. [[CrossRef](#)]
19. Xue, M.; Zhang, Y.; Kang, Y.; Yi, Y.; Li, S.; Liu, F. Full feedforward of grid voltage for discrete state feedback controlled grid-connected inverter with LCL filter. *IEEE Tran. Power Electron.* **2012**, *27*, 4234–4247. [[CrossRef](#)]
20. IEEE Standards Board. *IEEE Standard for Interconnecting Distributed Resources with Electric Power Systems*; IEEE Standard: Piscataway, NJ, USA, 2003; pp. 1547–2003.
21. Yoon, S.J.; Kim, K.H. Multiloop current control for an inductive–capacitive–inductive-filtered grid-connected inverter with frequency-adaptive capability under distorted grid environment. *IET Power Electron.* **2019**, *12*, 1521–1531. [[CrossRef](#)]
22. Texas Instrument. *TMS320F28335 Digital Signal. Controller (DSC)—Data Manual*; Texas Instrument: Dallas, TX, USA, 2008.

Publisher’s Note: MDPI stays neutral with regard to jurisdictional claims in published maps and institutional affiliations.



© 2020 by the authors. Licensee MDPI, Basel, Switzerland. This article is an open access article distributed under the terms and conditions of the Creative Commons Attribution (CC BY) license (<http://creativecommons.org/licenses/by/4.0/>).